

Fast and Accurate Detection of Action Potentials From Somatic Calcium Fluctuations

Takuya Sasaki,¹ Naoya Takahashi,¹ Norio Matsuki,¹ and Yuji Ikegaya^{1,2}

¹Laboratory of Chemical Pharmacology, Graduate School of Pharmaceutical Sciences, The University of Tokyo; and ²Precursory Research for Embryonic Science and Technology, Japan Science and Technology Agency, Tokyo, Japan

Submitted 25 January 2008; accepted in final form 1 July 2008

Sasaki T, Takahashi N, Matsuki N, Ikegaya Y. Fast and accurate detection of action potentials from somatic calcium fluctuations. *J Neurophysiol* 100: 1668–1676, 2008. First published July 2, 2008; doi:10.1152/jn.00084.2008. Large-scale recording from a population of neurons is a promising strategy for approaching the study of complex brain functions. Taking advantage of the fact that action potentials reliably evoke transient calcium fluctuations in the cell body, functional multineuron calcium imaging (fMCI) monitors the suprathreshold activity of hundreds of neurons. However, a limitation of fMCI is its semi-manual procedure of spike extraction from somatic calcium fluctuations, which is not only time consuming but is also associated with human errors. Here we describe a novel automatic method that combines principal-component analysis and support vector machine. This simple algorithm determines the timings of the spikes in calcium fluorescence traces more rapidly and reliably than human operators.

INTRODUCTION

Monitoring the dynamics of large neuronal ensembles is indispensable to unveil the activity patterns hidden in a neural circuit. One of the promising techniques for this is functional multineuron calcium imaging (fMCI), an optical recording technique that reconstructs the activity pattern of numerous neurons from the calcium fluorescence signals of their cell bodies by taking advantage of the fact that action potentials evoke somatic calcium transients. fMCI also identifies the physical positions of active and inactive cells during the observation period and can be applied to both invertebrate and vertebrate animals *in vivo* (Dombeck et al. 2007; Kerr et al. 2005, 2007; Ohki et al. 2005, 2006; Sato et al. 2007; Sohya et al. 2007; Stosiek et al. 2003) as well as to *in vitro* brain preparations (Cossart et al. 2003; Crepel et al. 2007; Ikegaya et al. 2004; MacLean et al. 2005; Mao et al. 2001; Sasaki et al. 2006, 2007).

Despite the wide applicability of fMCI, there are still some technical problems. The spike reconstruction procedure, which is time consuming, inevitably includes artificial errors. To resolve this problem, several methods have been used to automatically reconstruct neuronal events from raw fluorescence signals. They include template-matching algorithms (Kerr et al. 2005), reverse correlation (Ramdya et al. 2006), threshold crossing of $\Delta F/F$ and/or its derivative (Cossart et al. 2003; Ikegaya et al. 2004) and a novel detection algorithm for rodent cortex *in vivo* (Greenberg et al. 2008). In addition, calcium transient deconvolution (Yaksi and Friedrich 2006)

and its relevant, more flexible algorithm (Moreaux and Laurent 2007) have been developed to estimate the firing rates from calcium fluctuations. These methods are simple and convenient but may sometimes be too sensitive to optical noises. Moreover the thresholds for defining neuronal events must be determined empirically (or arbitrarily). In the present study, we have devised a new computational framework that can reconstruct the spike timings more precisely without being affected by any subjective factor.

To this end, we first scrutinized the properties of action potential-evoked calcium transients in hippocampal slice cultures. Although the basic waveforms of calcium transients have been characterized in the soma (Canepari et al. 1999; Lips and Keller 1999; Smetters et al. 1999) and dendrites (Helmchen et al. 1996; Markram et al. 1995) of a neuron intracellularly loaded with fluorophore through a patch pipette, the properties of the calcium transients in acetoxymethyl ester (AM)-loaded neurons remain unknown. Here we addressed the following issues: 1) loading efficiency of Oregon green 488 BAPTA-1AM (OGB-1AM), one of the most widely used calcium indicators in fMCI, into cultured slice preparations; 2) the cellular calcium source in calcium transients; and 3) the relationship between calcium transient kinetics and the number and frequency of spikes at the generally used low frame rates of 10–50 Hz. Information on how individual calcium transients are linked to spikes is essential not only for establishing a spike detection algorithm but also for properly interpreting the fMCI data. Through these investigations, we sought to develop a spike detection algorithm by combining principal-component analysis (PCA) and support vector machine (SVM).

METHODS

Slice preparation

Hippocampal slice cultures were prepared from postnatal day 7 Wistar/ST rats (SLC, Shizuoka, Japan) as previously described (Koyama et al. 2007), according to National Institutes of Health guidelines for the care and safety of laboratory animals. Briefly, rat pups were chilled with ice and decapitated, and the brains were removed and horizontally cut into 300- μ m-thick slices using a DTK-1500 vibratome (Dosaka, Kyoto, Japan) and were immersed in aerated, ice-cold Gey's balanced salt solution (Invitrogen, Garthursburg, MD) supplemented with 25 mM glucose. Entorhino-hippocampal stumps were cultivated on Omnipore membrane filters (JHWP02500; Millipore, Bedford, MA) that were laid on plastic ring disks. The cultures were fed with 1 ml of 50% minimal essential medium, 25% Hanks' balanced salt

Address for reprint requests and other correspondence: T. Sasaki, Laboratory of Chemical Pharmacology, Graduate School of Pharmaceutical Sciences, The University of Tokyo, Tokyo 113-0033 Japan (E-mail: ff077204@mail.ecc.u-tokyo.ac.jp).

The costs of publication of this article were defrayed in part by the payment of page charges. The article must therefore be hereby marked "advertisement" in accordance with 18 U.S.C. Section 1734 solely to indicate this fact.

solution (Invitrogen), 25% horse serum (Cell Culture Laboratory, Cleveland, OH), and antibiotics in a humidified incubator at 37°C in 5% CO₂. The medium was changed every 3.5 days.

Functional multineuron calcium imaging

On days 7–14 *in vitro*, the slices were washed three times with oxygenated artificial cerebrospinal fluid (ACSF) consisting of (in mM) 127 NaCl, 26 NaHCO₃, 3.3 KCl, 1.24 KH₂PO₄, 1.0 MgSO₄, 1.0 CaCl₂, and 10 glucose. They were transferred into a dish (35 mm diam) containing 2 ml of the dye solution and were incubated for 1 h in a humidified incubator at 37°C under 5% CO₂ (Ikegaya et al. 2005; Morita et al. 2003; Takahashi et al. 2007). The dye solution was ACSF containing 10 μl of 0.1% OGB-1AM/DMSO (Invitrogen), 2 μl of 10% Pluronic F-127/DMSO (Invitrogen), and 2 μl of 5% Cremophor EL/DMSO (Sigma, St. Louis, MO). After being washed, the slices were incubated at room temperature for >30 min and were mounted in a recording chamber perfused with ACSF at 32°C. The fluorophores were excited at 488 nm using an argon-krypton laser (5–10 mW, 641-YB-A01; Melles Griot, Carlsbad, CA) and were visualized using a 507-nm long-pass emission filter. Images (653 × 492 pixels = 383 × 289 μm; 512 × 512 pixels = 520 × 520 μm; 14–16 bit intensity) were captured at 10–50 frame/s using a Nipkow disk confocal microscope (CSU10/CSU-X1; Yokogawa Electric, Tokyo, Japan), cooled CCD cameras (Cascade; Roper Scientific, Tucson, AZ; iXON DV887; Andor, Belfast, Northern Ireland, UK), upright microscopes (ECLIPSE FN1; Nikon, Tokyo, Japan; AxioSkop2; Zeiss, Oberkochen, Germany) equipped with water-immersion objectives (×20, 0.5 numerical aperture (NA); ×40, 0.8 NA, Achroplan, Zeiss; ×16, 0.8 NA, CFI75LWD16XW, Nikon), and Metamorph software (Molecular Devices, Union City, CA). Fast Z-dimension scanning along the optical axis was performed with a piezo actuator (Physik Instrumente) and its control unit (PCU100, Andor). Image compensation was not done.

The cell bodies of neurons were identified by eye to put the regions of interest (10-μm-radius circles) in which the average fluorescence was measured. For each cell, the change in somatic fluorescence ($\Delta F/F$) was calculated as $(F_1 - F_0)/F_0$, where F_1 is the fluorescence intensity at any time point, and F_0 is the average baseline fluorescence intensity before and after the 10-s recording epoch. This normalization with a 20-s epoch around the target frame is needed to compensate photobleaching.

Two-photon imaging

Images of cells stained by the dyes were visualized using a two-photon laser scanning system based on a mode-locked Ti:sapphire laser with a 100-fs pulse width, 80-MHz pulse frequency, and 920-nm wavelength (Maitai; Spectra Physics, Mountain View, CA) and mounted on an upright microscope (BX61WI; Olympus). The excitation light was focused using a water-immersion objective (×20, 0.95 NA, XLUMPlanFI/IR; Olympus). The emitted fluorescence was detected using photomultiplier tube detectors (PMTs; Direct Detection System; Olympus).

Electrophysiological recording

Patch-clamp recordings from CA3 pyramidal cells were carried out using an Axopatch 700B amplifier (Molecular Devices, Union City, CA). For loose cell-attached and whole cell recordings, borosilicate glass pipettes (4–9 MΩ) were filled, respectively, with ACSF and an internal solution consisting of (in mM) 120 K gluconate, 20 KCl, 10 HEPES, 0.4 Na₂-GTP, and 4 Mg-ATP and 50 nM CaCl₂ (pH 7.2). OGB-1 potassium salt (Invitrogen) was dissolved in the intracellular solutions to attain a final concentration ranging from 1 to 200 μM. Signals were low-pass filtered at 1–2 kHz, digitized at 10 kHz, and analyzed using pCLAMP 9.2 software (Molecular Devices). All solutions were stored at –20°C, diluted immediately before use, and bath applied. The excitatory or inhibitory postsynaptic events were

automatically extracted based on a single criterion, namely, a current size >5 pA.

Nissl staining

After recording, the slice cultures were immersed in a mixture of 4% paraformaldehyde, 1% Triton X-100, and red or green NeuroTrace fluorescent Nissl (1:100; Invitrogen) in 0.1 M phosphate-buffered saline (PBS) for 1 h at room temperature.

Manual spike reconstruction

The spike times were manually reconstructed from the onset of the calcium transients using a custom-made software in Microsoft Visual Basic (Ikegaya et al. 2004).

Automatic spike reconstruction

Our automatic algorithm is composed of two steps, i.e., conditioning (learning) phase and test (spike detection) phase. In the conditioning phase, the parameters are tuned to give the most appropriate rate of spike detection from sample datasets. In the test phase, the algorithm with the best tuned parameters extracts spike signals from datasets different from those used in the conditioning phase. The data used for conditioning was collected from 10 cells. The average recording period was 312 ± 137 s (same as in Figs. 4 and 5; 1,782 spike signals and 2,000 nonspike signals). All routines were written in Matlab (The Math Works).

CONDITIONING PHASE. We used 1,782 spike signals and 2,000 nonspike signals, which were obtained simultaneously with calcium imaging and loose patch-clamp recording. For each trace, we extracted a portion of calcium fluorescence trace from t_s (in ms) to t_e (in ms) relative to the first spike frame (F_{spike}) and defined each as a sample vector \vec{S} (see Fig. 5A, top). Note that t_s and t_e represent negative and positive values, respectively. Thus the vector length N was equal to $1 + (t_e - t_s)/f$, where f denotes the interframe interval (here, $f = 100$ ms). Then each sample vector was normalized such that all components of the vector were between 1 and 0. These components reflect the characteristic shape of the calcium transient with a sharp rise followed by a slow decay.

Next, one dimension was added in the vector, as follows

$$\vec{S}(N+1) = [\vec{S}(F_{\text{spike}} + 1) + \vec{S}(F_{\text{spike}})]/2 - [\vec{S}(F_{\text{spike}} - 1) + \vec{S}(F_{\text{spike}} - 2)]/2$$

which corresponds to the difference in the fluorescence intensity before and after the spike times. At our sampling rates, it is conceptually equal to the amplitude of the calcium transient.

Using PCA, two principal dimensions were extracted from the set of vectors. To evaluate the degree of separation of the two distributions (with or without spikes) on the principle component (PC) coordinate (see Fig. 5B), we used Jensen-Shannon (JS) divergence, which quantifies the degree of dissimilarity between the two distributions. The coordinate system spanned by the first two PC components was divided into 50×50 grids in each of which the distribution probability of data points was calculated. The distributions of vectors with and without spikes were defined as p and q , respectively.

If the two probability distributions are given by p and q , respectively, JS is calculated in the following manner

$$JS(p, q) = \frac{1}{2} \left[D\left(p \left\| \frac{p+q}{2} \right.\right) + D\left(q \left\| \frac{p+q}{2} \right.\right) \right]$$

where D denotes the Kullback-Leiber divergence, i.e.

$$D(p||q) = \sum_i p_i \log \frac{p_i}{q_i}$$

The JS divergence assumes a value between 0 and log 2 with higher values indicating better separation. Unlike the Kullback-Leiber divergence, the JS divergence is symmetric between p and q .

Next, in the two PC coordinates, linear SVM was applied to determine the discriminant border between the two regions (Smola and Schölkopf 2004). The SVM-code is available at <http://www.kyb.tuebingen.mpg.de/bs/people/chapelle/primal/>. We defined the SVM score as the relative distance from each data point to the separating line as follows

$$\text{SVM score} = x'W^t + b$$

We repeatedly conditioned the SVM by modulating the vector w that is perpendicular to the best separating line and the intercept b in order that the SVM score assumes a positive value if the vector x contains spikes. Through the conditioning (or training) process, we obtained the most optimal parameters w and b with the following test phase.

TEST PHASE. From a time series of the fluorescent calcium trace $F(t)$, the windows that contain N data points around the focused time T (in ms) were successively slid along the time axis of the parent dataset and each was defined as a vector \vec{x}_T as follows

$$\vec{x}_T = [F(T + t_s), F(T + t_s + f), F(T + t_s + 2f), \dots, F(T), F(T + f), \dots, F(T + t_e - f), F(T + t_e)]$$

Similar to the conditioning phase, each vector component was normalized such that the maximum and minimum component values assumed 1 and 0, respectively. Further, one component was added to the vector as follows.

$$\vec{x}_T(N + 1) = [F(T + f) + F(T)]/2 - [F(T - f) + F(T - 2f)]/2$$

The vector was decomposed into two dimensions by PCA using the same eigenvectors as those used in the conditioning phase, and the SVM score was calculated using w and b .

At the points where the SVM scores assumed local maxima >0 , the vectors were defined as spike signals.

Statistics

We reported the data as the means \pm SD. The signal-to-noise (SN) ratio was defined as the amplitude of spike signals divided by the SD of fluorescence intensity in the trace, ANOVA Student's t -test, and

Tukey's test were performed to assess the significance of the differences. P values <0.05 were considered statistically significant.

RESULTS

Loading hippocampal cells with OGB-1AM

Hippocampal slice cultures were incubated in OGB-1AM solution, a membrane-permeable precursor of the membrane-impermeable calcium indicator OGB-1. OGB-1AM passively diffuses into cells through the plasma membrane and is converted to OGB-1 by intracellular esterase. OGB-1 fluorescence images were compared with *post hoc* staining with fluorescent Nissl, a neuron-specific marker (Fig. 1, *top*). Two-photon microscopic observation revealed that the loading efficiency gradually decreased as the Z depth increased and became almost zero at a depth of 100 μm underneath the surface of the slice preparation (Fig. 1, *bottom*). However, in case of neurons located within a depth of 50 μm , $88.3 \pm 2.5\%$ cells were labeled with OGB-1AM ($n = 4$ slices).

To estimate the intracellular OGB-1 concentration after AM-dye loading, we directly injected the OGB-1 potassium salt at different concentrations using patch-clamp pipettes (Fig. 2A). After maintaining whole cell configurations over 30 min to allow sufficient intracellular perfusion, images were obtained at multiple Z depths with an interval of 5 μm . The fluorescence intensity in the somatic region was averaged over individual images, and the maximum fluorescence intensity was used for estimation. The neurons that showed activity during image acquisition were discarded. The somatic fluorescence intensity almost linearly correlated with the intra-pipette OGB-1 concentration (Fig. 2A, *right*, $n = 2-3$ cells each). Then the brightness of neurons that had been intracellularly perfused with OGB-1 were compared with that of the AM-loaded neurons. Under the assumptions that $[\text{Ca}^{2+}]_i$ at the resting membrane potential is equivalent to that in the pipette (50 nM) (Helmchen et al. 1996) and that OGB-1 was homogeneously distributed into the cytoplasmic space, we estimated the intracellular concentrations of OGB-1 in the AM-loaded neurons and found that they ranged from 7 to 50 μM (shaded area of Fig. 2A, *right*).

OGB-1 is a high-affinity indicator with a K_d value of 170 nM for calcium ions (Takahashi et al. 1999; Thomas et al. 2000). Thus the loaded OGB-1 may function as a $[\text{Ca}^{2+}]_i$ reporter and

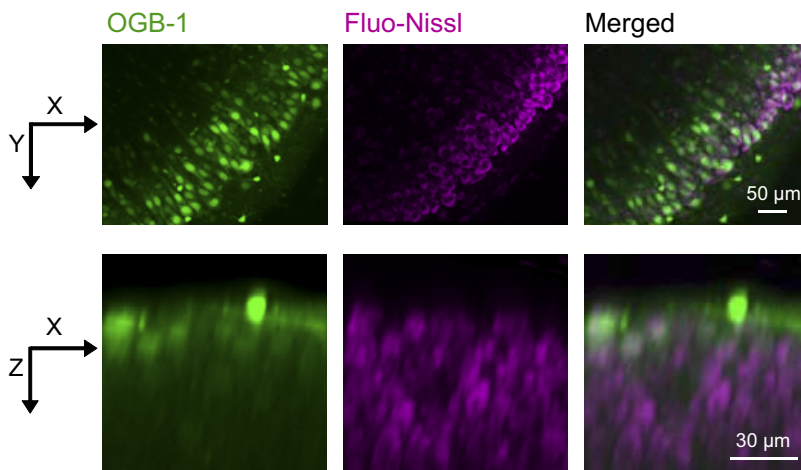


FIG. 1. Loading of the cultured hippocampal slices with calcium-sensitive acetoxymethyl ester (AM) indicators. *Top*: horizontal X-Y views of 1-photon images of the CA3 region of a hippocampal slice culture loaded with Oregon green 488 BAPTA-1AM (OGB-1AM, *left*) and stained with *post hoc* fluorescent Nissl in the same field (*middle*). These images have been superimposed on each other in the *right* panel. *Bottom*: orthogonal X-Z views obtained by 2-photon microscopy.

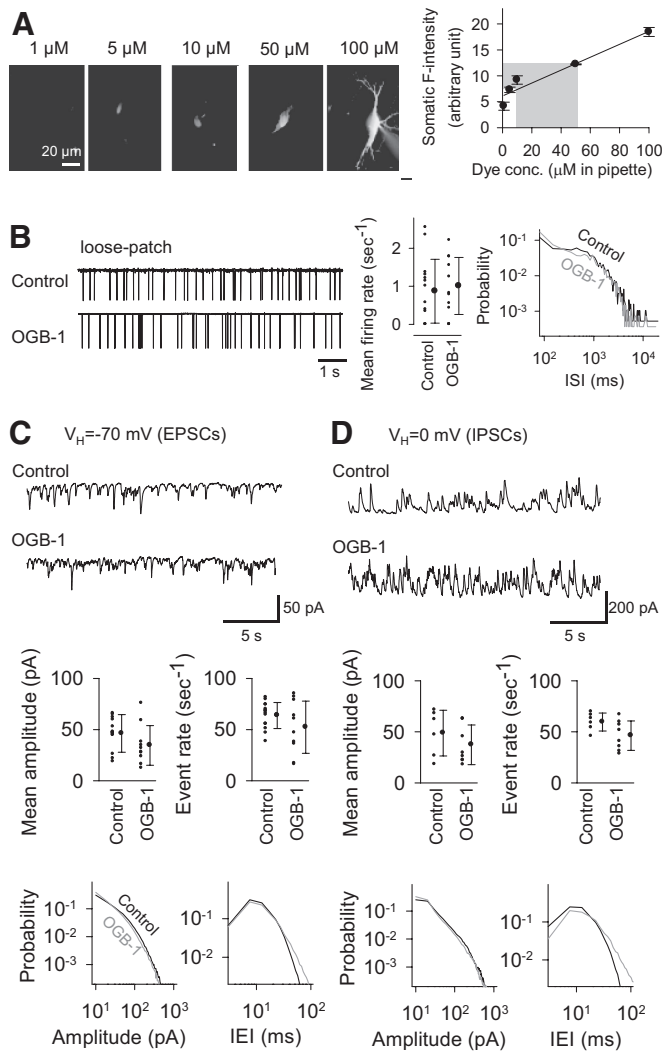


FIG. 2. Absence of effect of loading of calcium fluorophores on neuronal activity. *A, left*: fluorescence images of the CA3 pyramidal neurons that had been intracellularly loaded with 1, 5, 10, 50, and 100 μM OGB-1 through patch-clamp pipettes. *Right*: the somatic fluorescence intensity increased linearly with the concentration of the injected calcium indicators. The shaded area corresponds to the range of fluorescence intensity observed in neurons loaded with OGB-1AM. *B, left*: the action potentials monitored by loose-patch recording from the unloaded neurons (control) and the OGB-1AM-loaded neurons (OGB-1). *Middle*: the average firing frequency did not differ significantly between the control and the OGB1-treated groups (Student's *t*-test, $t_{23} = 0.036$; $P = 0.97$, $n = 13$ neurons each). *Right*: distribution of the interspike intervals in the control and OGB-1AM-loaded neurons (Kolmogorov-Smirnov test; $P > 0.05$). *C, top*: the representative traces of whole cell recordings from the unloaded neurons (control; $n = 14$ neurons) and the OGB-1AM-loaded neurons (OGB-1; $n = 10$ neurons). Excitatory postsynaptic currents (EPSCs) were recorded at -70 mV. *Middle*: the average amplitudes (*left*; Student's *t*-test, $t_{22} = 1.66$; $P = 0.11$) and frequencies (*right*; Student's *t*-test, $t_{22} = 1.45$; $P = 0.16$) of the postsynaptic events. *Bottom*: the distributions of the individual amplitudes (*left*; Kolmogorov-Smirnov test, $P > 0.05$) and interevent intervals (*right*; Kolmogorov-Smirnov test, $P > 0.05$). *D*: data for inhibitory postsynaptic currents (IPSCs; control, $n = 6$ neurons and OGB-1, $n = 7$ neurons). The average amplitudes (Student's *t*-test, $t_{12} = 1.19$; $P = 0.26$) and frequencies (Student's *t*-test, $t_{12} = 2.00$; $P = 0.07$) of postsynaptic events did not differ significantly between the 2 groups. Also there were no significant differences between both groups with regard to the distributions of the amplitudes (Kolmogorov-Smirnov test, $P > 0.05$) and interevent intervals (Kolmogorov-Smirnov test, $P > 0.05$).

as a calcium chelator. To examine whether OGB-1AM loading disturbs the nature of neuronal firing activity, we performed loose-patch recordings from randomly selected AM-loaded neurons and recorded spontaneously occurring action potentials (Fig. 2*B*). The average firing rate did not differ significantly between the OGB-1-loaded and unloaded cells (Fig. 2*B, middle*); moreover, the distribution of the interspike intervals also did not differ significantly between these two groups (Fig. 2*B, right*). In addition, we carried out whole cell voltage-clamp recording to record spontaneous synaptic inputs (Fig. 2, *C* and *D, top*). OGB-1AM loading did not alter the mean event rate, the amplitude of spontaneous excitatory or inhibitory postsynaptic events (Fig. 2, *C* and *D, middle*), or the distribution of the amplitudes and the interevent intervals of the postsynaptic events (Fig. 2, *C* and *D, bottom*). These results suggest that OGB-1AM loading per se does not alter the level or pattern of neuronal electrical activity.

Relationship between action potentials and somatic calcium spikes

Simultaneous recordings of membrane potential and somatic calcium fluorescence showed that somatic calcium transients strictly reflected the action potentials (Fig. 3*A, left*), whereas somatic fluorescence did not change with subthreshold fluctuations in the membrane potential (Fig. 3*A, right*). This implies that the timings of the action potentials can be reconstructed based on the onset timings of individual calcium transients without being disturbed by subthreshold synaptic inputs or ongoing membrane fluctuations.

We sought to determine the source of spike-evoked calcium influx in our cultured hippocampal neurons. Calcium transients evoked by current injection through the OGB-1-loaded pipettes were compared before and after bath application of several pharmacological reagents. Calcium transients were almost completely abolished by 100 μM Cd^{2+} , a broad spectrum calcium channel inhibitor (Fig. 3*B, left*). The $\Delta F/F$ amplitude was decreased to $4.8 \pm 10.6\%$ in the Cd^{2+} -treated neurons ($n = 5$). Thus the calcium transients appeared to depend on

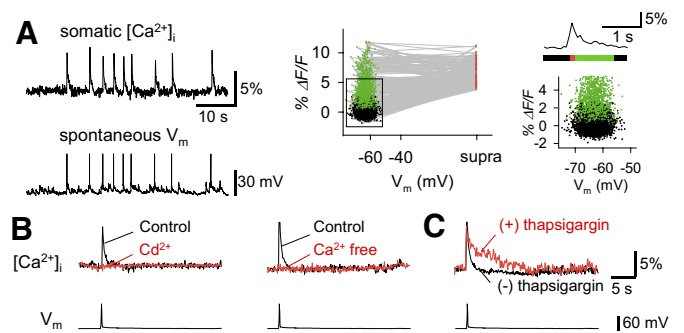


FIG. 3. Characterization of the somatic calcium transients. *A, left*: simultaneous calcium imaging sampled at a frame rate of 50 Hz (*top*) and whole cell recording (*bottom*) from a hippocampal CA3 pyramidal neuron. Calcium transients coincided with action potentials. *Middle*: the calcium fluorescence intensity was plotted against the membrane potential. The label "Supra" indicates action potentials. Red, green, and black dots represent the points in the spike frames, subsequent 1-s frames, and others, respectively. The boxed region has been expanded in the *right panel*. *B*: the representative spike-induced calcium transients before (control) and after bath application of 100 μM Cd^{2+} (*left*; $n = 5$) and calcium-free extracellular solution (*right*; $n = 4$). *C*: calcium traces of thapsigargin-treated and intact slices were compared ($n = 5$ neurons each).

extracellular calcium influx through voltage-dependent calcium channels. Consistent with this, calcium transients did not occur in a calcium-free solution (Fig. 3*B*, right). The $\Delta F/F$ amplitude was decreased to $1.2 \pm 0.9\%$ in the calcium-free neurons ($n = 4$).

We also examined whether calcium release from endogenous Ca^{2+} stores contributes to the calcium transients (Fig. 3*C*). Neurons were treated for >30 min with thapsigargin, a Ca^{2+} -ATPase inhibitor, to deplete calcium in the endoplasmic reticulum. Thapsigargin did not significantly alter the amplitude of the calcium transients. The $\Delta F/F$ amplitude was $5.4 \pm 1.3\%$ in the control and $5.0 \pm 1.7\%$ in thapsigargin-treated neurons ($n = 4$). However, thapsigargin prolonged the recovery of the calcium transients. The decay time constant was 484 ± 123 ms in the control and $6,750 \pm 2,217$ ms in the thapsigargin-treated neurons. These results indicate that calcium release from the internal stores is not required for the rapid surge of a calcium transient; however, thereafter, the intercellular Ca^{2+} -ATPase-dependent calcium clearance, at least in part, contributes to the pattern of calcium decay.

We next addressed the relationship between the number of action potentials in a burst and somatic calcium increase. All data were collected from the calcium transients obtained during spontaneous activity. As shown in Fig. 4*A*, single spikes evoked clearly visible calcium transients, whereas at frequencies of >5 Hz, the individual spikes in bursts were inseparable in the calcium traces and instead evoked single large events due to the temporal accumulation of calcium transients owing to their slow decay kinetics.

The amplitude of calcium transients increased as a function of the average spike counts (Fig. 4*B*, left, red circles); however, it varied largely between the transients even if the transients had the same number of spikes (black dots). The decay time

constant after calcium transients was not significantly different among neurons ($n = 10$ cells, data not shown). The decay also did not depend on the number of spikes involved in the events (Fig. 4*B*, right). The variance of the amplitudes appeared to arise, at least in part, from the intraburst spike timings because the sizes of the calcium transients also correlated positively with the spike frequencies (Fig. 4*C*). Figure 4*D* depicts the sizes of the calcium transients on a pseudocolor scale in dimensions of spike numbers versus firing rates, indicating that the transient size depends on both parameters, that is, the same amplitude of calcium transients can be evoked by different sets of spike numbers and firing rates.

Conditioning of the spike detection algorithm with PCA and SVM

We developed a novel method to automatically detect the spike events using a machine learning algorithm. Although in the following analysis, we present results obtained from datasets recorded at a sampling rate of 10 Hz, similar results were obtained in the range from 10 to 50 Hz. In the first step, a part of the calcium trace was regarded as a time-series vector (Fig. 5*A*, top, see METHODS) and was decomposed into two dimensions by PCA. Data were plotted in a space of the first PC versus the second PC. For illustrative purposes, 1,782 randomly selected spike vectors and 2,000 nonspike vectors obtained from 10 cells are shown in Fig. 5*B*. The vectors with spikes (colored dots) and those without spikes (gray dots) tended to be scattered in different regions.

We attempted to determine the appropriate vector length, i.e., the length of the fluorescence trace segments around the focused spikes that should be clipped out of a parent trace. The optimal length is the length that yields the best separation between spike and nonspike vectors. We computed the JS divergences, which assess the degree of separation, by performing the entire PCA procedure against various combinations of the start and end time points, i.e., t_s and t_e , respectively, relative to the focused spikes (Fig. 5*A*). The JS divergence peaked when the vectors were extracted from $t_s = -200$ ms (start) to $t_e = +400$ ms (end; Fig. 5*A*, bottom). In the following analysis, we used vectors with $t_s = -200$ ms and $t_e = +400$ ms.

We used linear SVM, a supervised machine learning algorithm, to determine the cutoff line that best separated the spike and nonspike vectors in the PC coordinate system. As the SVM is conditioned to judge whether the vectors contained spikes or not, it gradually learns to identify vectors with spikes. The average learning curve is shown in Fig. 5, *C* and *D*. In this analysis, the vectors used for SVM conditioning were not used for the subsequent detection tests. Bursts at spike rates >5 Hz were regarded as single events, and one frame error was allowed around the actual event time. We considered two types of errors: erroneous detection of a nonspike as a spike (false-positive) and erroneous oversight of a spike as a nonspike (false-negative). Both types of errors decreased as the number of vectors used for conditioning increased (Fig. 5*C*), and the learning was almost saturated at conditioning with 1,000 vectors (Fig. 5*D*).

We also conditioned SVM without PCA preprocessing of the vectors, that is, the original high-dimensional vectors were directly used for SVM conditioning. In this case, the total computation time spent for conditioning was 50–100% longer

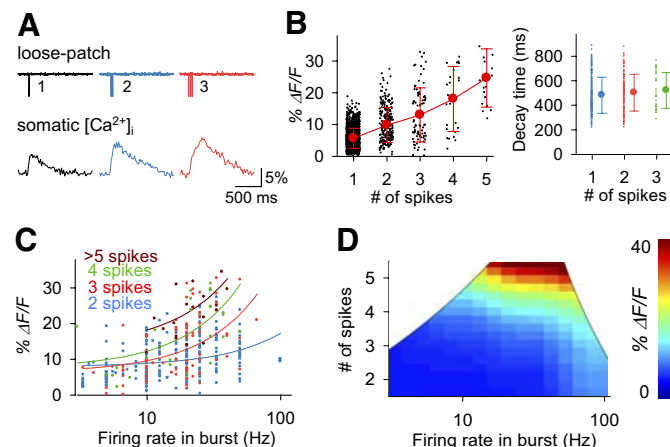


FIG. 4. The nonlinear relationship between burst-like spikes and somatic calcium dynamics. *A*: the representative somatic calcium traces induced by spontaneously occurring single (left), double (middle), and triple spikes (right) sampled at 50 Hz. Calcium transients evoked by relatively regular bursts at ~50 Hz were selected. *B*, left: the relationship between the number of action potentials and the amplitude of calcium transients sampled at 10–50 Hz rate ($n = 1,782$ transients from 10 cells). Right: the relationship between the number of action potentials and the decay time constant of calcium transients. Individual data are plotted as dots, and their average with the SDs are shown on the side. *C*: the relationship between the spike frequency within the bursts and the amplitude of the calcium transients. The colors correspond to the number of spikes involved in bursts. *D*: pseudocolor representation of the amplitudes of the calcium transients. The horizontal and vertical axes represent the firing rates and the number of spikes, respectively.

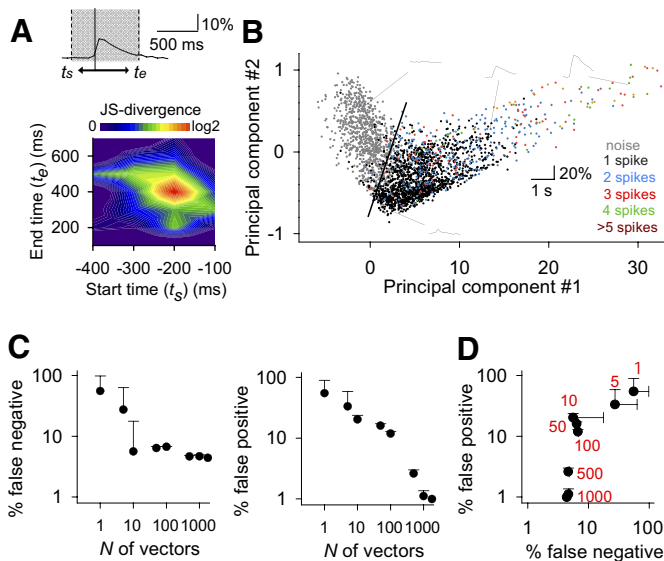


FIG. 5. Conditioning the principal component analysis (PCA)-support vector machine (SVM) algorithm for spike detection from somatic calcium fluctuations. **A**: a short-range portion from t_s to t_e (shaded area) was extracted from a raw fluorescence trace and was defined as a vector (*top*). The Jensen-Shannon (JS) divergence was used to quantify the degree of separation between the vectors with and without spikes (*bottom*). The horizontal axis and vertical axis represent the start (t_s) and end time (t_e), respectively, relative to the focused frame. The maximal separation was marked at $t_s = -200$ and $t_e = +400$. **B**: the vectors with $t_s = -200$ and $t_e = +400$ were decomposed by PCA, and their 1st and 2nd principal components are illustrated in the PC1 vs. PC2 coordinate system. The spike vectors are indicated in color ($n = 1,782$ calcium transients obtained from 10 cells), whereas the nonspike vectors are indicated in gray ($n = 2,000$). The colors correspond to the number of spikes in the vectors. The data were collected from 10 cells. **C**: the learning curve of SVM. Both false-positive (*left*) and false-negative (*right*) rates decreased as a function of the number of sample vectors exposed to SVM. **D**: the same data were replotted in terms of the false-positive vs. the false-negative rates. The numbers in red indicate the number of sample vectors used for SVM conditioning.

as compared with the time spent with the PCA-SVM algorithm, and the error rates after learning were 10–20% higher (data not shown). Thus the data compression with PCA prior to SVM conditioning enhances the learning efficacy of SVM.

Fast and accurate reconstruction of spike timings from calcium signals

The SVM score (see METHODS) quantifies the distance from a given vector to the cutoff line that separates the spike and nonspike vectors, representing the likelihood that the vector contains spike(s). Spike times are determined as the >0 local maxima of the SVM score. The representative fluorescence trace from two neurons and their corresponding SVM scores are shown in Fig. 6. Note that these traces were obtained from neurons that had not been used in SVM conditioning. Spike times detected automatically with the PCA-SVM algorithm are indicated (● along the SVM score). They corresponded well, although not perfectly, to the actual times of the spikes monitored by loose-patch recording (Fig. 6, *A* and *B*, *bottom*). The error rates are shown in each *top right* panel. We compared the detection results between the PCA-SVM algorithm and four trained human operators in our laboratory. In our slice preparations, ~70% of the neurons generated stereotypical calcium transients with high signal-to-noise (SN) ratios, as shown in Fig. 6A (SN ratio = 48). In these cases, the detection error rates

by both our algorithm and by the human operators were low (Fig. 6A). Other neurons, however, exhibit obscure calcium transients, presumably because of the high firing rates or out-of-focus signals as shown in Fig. 6B (SN ratio = 12). In these cases, the false-positive and false-negative error rates increased to ~40% in the case of the human operators; however, the PCA-SVM algorithm could still find spikes with error rates of $<10\%$. The *bottom right* histograms represent the distributions of the detected events around the actual spike

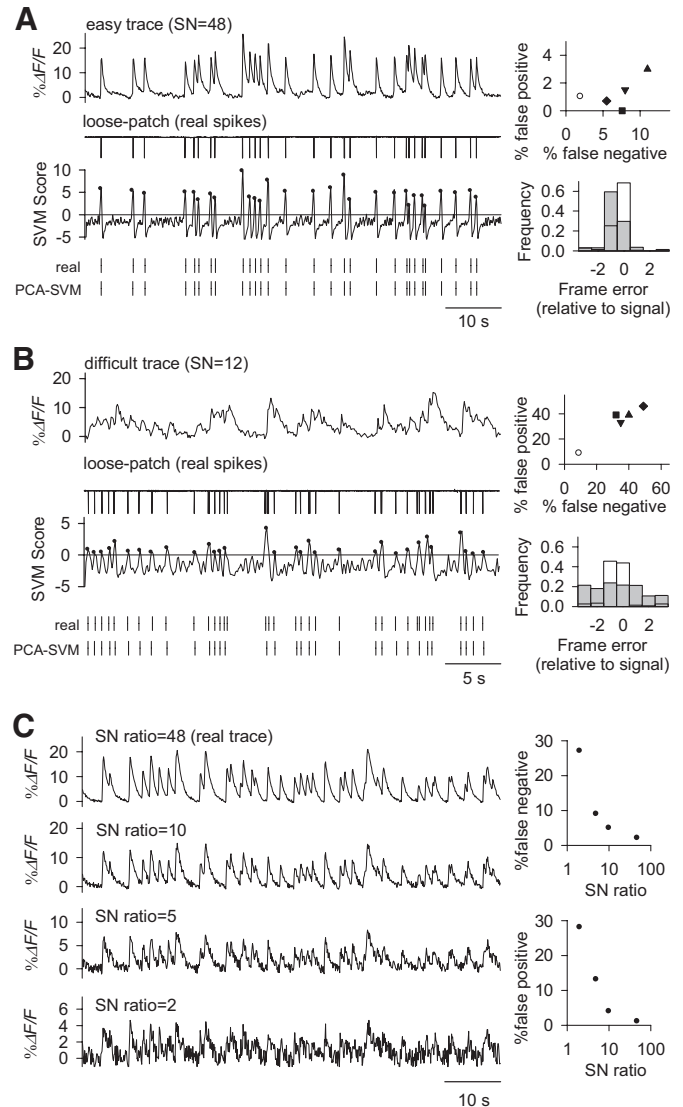


FIG. 6. Comparison of spike extraction with the computation performed by human operators. Fluorescence traces that were easy (*A*) or difficult (*B*) for human operators to interpret were compared. Somatic calcium signals sampled at 10 Hz, and the corresponding actual spike trains (*top*) were simultaneously recorded. *Middle*: the SVM score at the given frames. ●, events automatically detected using the PCA-SVM algorithm. The activity patterns reconstructed by PCA-SVM algorithm were compared with the real spike trains in the bottom panel. *Top right*: the false-positive (*y* axis) and false-negative (*x* axis) rates. The open circle indicates the score of the PCA-SVM algorithm. For comparison, the results of computation performed by 4 human operators (*BAN*, *HMW*, *NTG*, and *USA*) are shown as closed symbols in the same panels. *Bottom right*: histograms represent the distributions of the frames detected by the PCA-SVM algorithm (□) and by manual computation (▣) relative to the actual spike times. *C*, *left*: white noise was added to representative traces (the SN ratio of 48) in order that the SN ratios were 10, 5, and 2. *Right*: the false-negative (*top*) and false-positive (*bottom*) rates increased as the SN ratios decreased.

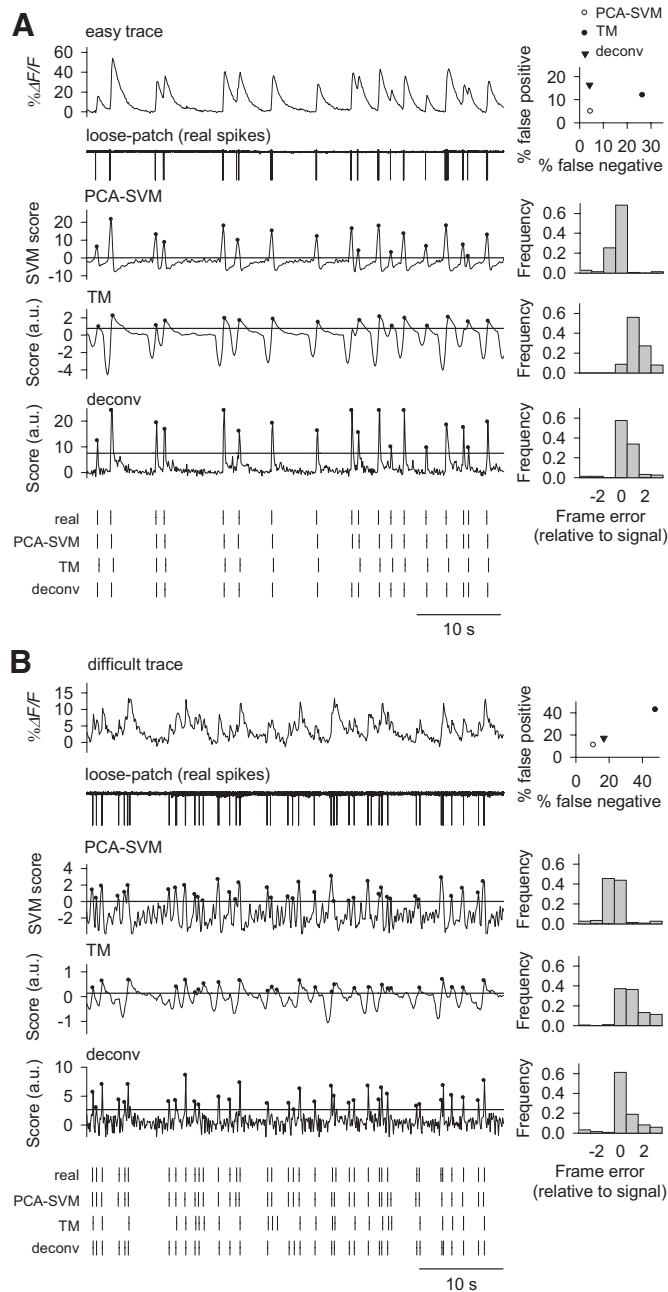


FIG. 7. Comparison of detection results using template-matching and deconvolution algorithms. Fluorescence traces that were easy (A) or difficult (B) to interpret were compared. Somatic calcium signals and their corresponding actual spike trains (top) were simultaneously recorded. Middle: the calculated scores at the given frames using the PCA-SVM, template-matching (TM), and deconvolution (deconv) algorithms. The activity patterns reconstructed by the algorithms were compared with the real spike trains in the bottom panel. Right: the scores of PCA-SVM (○), template matching (●), and deconvolution (▼). For details, see the legend of Fig. 6.

timings, indicating that the algorithm determined the timings of 40–60% events in the correct frames. Moreover, the PCA-SVM algorithm and human operators had different working speeds. Even in the “easy” case shown in Fig. 6, the human operators required 188 ± 49 s to complete spike detection, whereas the algorithm completed the task in 14 ms with a mass-produced 1-GHz desktop computer.

To examine the robustness of the PCA-SVM algorithm against the SN ratio, we artificially added white noise to the raw fluorescence trace. As the SN ratio decreased, the error rates increased (Fig. 6C). At a SN ratio of >10 , our algorithm worked with an error rate of $<10\%$.

We next compared the spike detection power of our algorithm with that of the other existing methods. We employed two representative algorithms, i.e., template matching (Kerr et al. 2005) and deconvolution (Yaksi and Friedrich 2006). Both algorithms were run under the assumption of a calcium decay constant of 500 ms (see Fig. 4B). All calculations were done in accordance with the previous papers except that no image compensations (i.e., background subtraction, local averaging or filtering) were performed in advance. Their scores are shown in Fig. 7. In the template-matching and deconvolution algorithms, we had to arbitrarily determine a threshold for spike detection. We defined them to minimize the error rates for individual trace. This optimization process could be disadvantageous as compared with our entirely automatic algorithm because all parameters in our algorithm were maintained across traces and not optimized for every trace. Even in these cases, our algorithm showed better spike detection rates than those the template-matching and deconvolution algorithms (Fig. 7). The most plausible reason seemed to be that these methods more frequently picked incorrect frames before or after actual spike timings (>2 frames) compared with PCA-SVM algorithm (right histogram). Similar results were obtained in other six neurons. Incidentally, the computation time did not differ much among these algorithms.

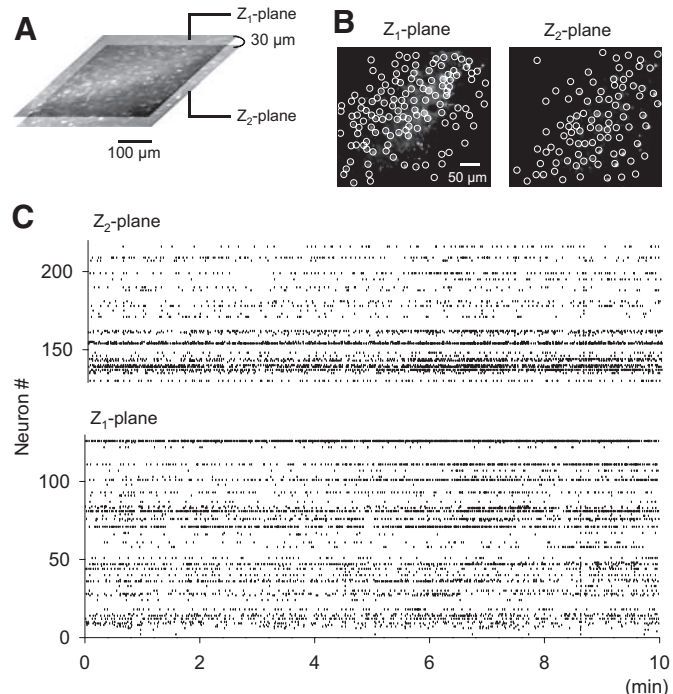


FIG. 8. Large-scale reconstruction of spike events using functional multineuron calcium imaging (fMCI). A: Ismages of the hippocampal CA3 region were fast-scanned from 2 confocal Z planes separated by a distance of $30 \mu\text{m}$ with a piezoelectric focusing element attached to an objective. The activity was monitored at 10 Hz for each plane. B: the locations of the 127 neurons in the Z1 plane and the 91 neurons in the Z2 plane. C: the automatically reconstructed spatiotemporal pattern of spontaneous activity of a total of 218 neurons using the PCA-SVM algorithm. ●, a single event.

Finally, we showed an example of large-scale reconstruction of multineuronal spike trains. The spontaneous activity of a CA3 network was imaged from two different Z planes, each at 10 Hz, using a fast piezoelectric focusing element (Göbel et al. 2007) (Fig. 8). The Z_1 and Z_2 planes contained 127 and 91 neurons, respectively (Fig. 8B). A rasterplot was reconstructed using the PCA-SVM algorithm (Fig. 8C). With the automatic algorithm, the time spent for reconstructing the whole network activity was reduced from a few hours (manual) to a few seconds (automatic).

DISCUSSION

Under our experimental conditions, $\sim 90\%$ of the Nissl-positive cells within a distance of 50 μm from the slice surface were loaded with OGB-1AM. Thus OGB-1AM permeated through the brain tissues up to a depth of $\sim 50 \mu\text{m}$, which happens to be almost equal to the Z depth accessible with a one-photon laser beam used in spinning-disk confocal microscopy. The intracellular concentration of AM-loaded OGB-1 seemed to be tens of micromoles. Although this concentration was enough to detect single action potentials, it did not seem to alter neuronal excitability. Suprathreshold activity induced calcium transients, whereas subthreshold synaptic activity alone did not seem to elicit calcium elevation in the cell body. This is probably because synaptic activity occurs at synaptic sites that are away from the cell body, whereas action potentials are initiated in the vicinity of cell body.

Because of the slow decay of the calcium transients, a series of action potentials with narrow interspike intervals produces calcium accumulation that overlaps the decay of previous calcium spikes (Canepari et al. 1999; Helmchen et al. 1996). Some studies have attempted to reconstruct spike counts (or frequencies) from raw $\Delta F/F$ signals. This requires an assumption that the calcium transient amplitudes strictly correlate with the spike counts (Feinerman and Moses 2006; Murayama et al. 2005). In general, however, neurons emit burst-like spike trains with variable spike counts and frequencies, and we found that both the spike count and frequency influence calcium dynamics in a nonlinear intermixed manner. Thus even if we consider the entire changes of $\Delta F/F$, one cannot simultaneously know the firing rate and the number of spikes within a burst (< 5 Hz), at least at the frame rates (10–50 Hz).

The spike reconstruction processes used in fMCI experiments has practical problems. The most elementary method to detect the neuronal events is by visual inspection. This manual operation is time consuming, laborious and may be subjective. As we demonstrated, human eyes are indeed inaccurate and are often biased, inevitably producing errors. To improve the detection process, we have created a new algorithm that focuses on specific segments around the peaks of $\Delta F/F$ signals and picks up spike events with the help of a combination of PCA and SVM. The spike detection power of this algorithm was maximal when the fluorescence trace segments were sampled from $t_s = -200$ ms to $t_e = +400$ ms relative to the focused frame, i.e., the assumed spike timings. The t_e value is reasonably similar to the decay constant of the calcium transients.

Not only was the computation time of the PCA-SVM algorithm $> 10,000$ times shorter than that of the manual computation performed by human operators, but the error of the

PCA-SVM algorithm was also a few times smaller than that of manual computation. This implies that manual processes are unnecessary and should be excluded as much as possible. The errors committed by our algorithm were fewer than those by template-matching (Kerr et al. 2005) and deconvolution (Yaksi and Friedrich 2006). Unlike template-matching, our method takes both the absolute $\Delta F/F$ amplitude of the calcium transient and its stereotyped decay into consideration. The dual parameters are thought to improve the detection power. Deconvolution may be suitable for reconstructing the firing rate in the neurons that emit continuous spikes at frequencies of > 10 Hz and have long decay constants of calcium transients (3–6 s) (Yaksi and Friedrich 2006). But in mammalian excitatory cells such as hippocampal neurons, which usually generate temporally sparse (< 1 Hz) firing activities and a short calcium decay constant (0.5–1 s), deconvolution may fail to detect precise spikes. A more crucial difference between these methods and ours, however, is the degree of subjective factors. In the template-matching and deconvolution algorithm, one needs to empirically define a threshold to extract neuronal events. This manual process is quite arbitrary and is subject to human bias. In this regard, our algorithm automatically finds the optimal line that separates the spikes during SVM conditioning, and the SVM score is defined in order that the detection threshold is zero. On the other hand, this could also be considered as a drawback of our algorithm—one first needs to condition the algorithm with at least many signals (we used 1,000) and thus has to prepare these fluorescence traces in advance.

As hippocampal neurons in cultured slices showed relatively homogenous calcium dynamics (for example, the decay time constant was similar among neurons), the parameters tuned with datasets of only 10 sample cells could be applied to detection for other neurons. But it should be noted that the parameters optimized in our study may not be directly applicable to other experimental systems that include different brain regions or different preparations. The PCA-SVM algorithm itself, however, is simple enough that one can easily optimize the parameters. The Matlab code of SVM is freely available at the website described in the Methods. Please contact the corresponding author (T. Sasaki; e-mail: ff077204@mail.ecc.u-tokyo.ac.jp) for the parameters used in this study. Finally, we believe that this automatic algorithm does not merely enhance the applicability of fMCI but also may help signal detection in other on-line experiments.

ACKNOWLEDGMENTS

We thank Dr. Toshihiko Hosoya (RIKEN Brain Science Institute) for providing insight into the use of the support vector machine. We are also grateful to M. Fassler for critical comments on earlier versions of the manuscript.

GRANTS

This work was supported in part by a Grant-in-Aid for Scientific Research (18021008, 17689004) from the Japan Society for Promotion of Science.

REFERENCES

- Canepari M, Mammano F. Imaging neuronal calcium fluorescence at high spatiotemporal resolution. *J Neurosci Methods* 87: 1–11, 1999.
- Cossart R, Aronov D, Yuste R. Attractor dynamics of network UP states in the neocortex. *Nature* 423: 283–288, 2003.
- Crepel V, Aronov D, Jorquera I, Represa A, Ben-Ari Y, Cossart R. A paritition-associated nonsynaptic coherent activity pattern in the developing hippocampus. *Neuron* 54: 105–120, 2007.

- Dombeck DA, Khabba AN, Collman F, Adelman TL, Tank DW.** Imaging large-scale neural activity with cellular resolution in awake, mobile mice. *Neuron* 56: 43–57, 2007.
- Feinerman O, Moses E.** Transport of information along unidimensional layered networks of dissociated hippocampal neurons and implications for rate coding. *J Neurosci* 26: 4526–4534, 2006.
- Göbel W, Kampa BM, Helmchen F.** Imaging cellular network dynamics in three dimensions using fast 3D laser scanning. *Nat Method* 4: 73–79, 2007.
- Greenberg DS, Houweling AR, Kerr JN.** Population imaging of ongoing neuronal activity in the visual cortex of awake rats. *Nat Neurosci* 11: 749–751, 2008.
- Helmchen F, Imoto K, Sakmann B.** Ca²⁺ buffering and action potential-evoked Ca²⁺ signaling in dendrites of pyramidal neurons. *Biophys J* 70: 1069–1081, 1996.
- Ikegaya Y, Aaron G, Cossart R, Aronov D, Lampl I, Ferster D, Yuste R.** Synfire chains and cortical songs: temporal modules of cortical activity. *Science* 304: 559–564, 2004.
- Ikegaya Y, Le Bon-Jego M, Yuste R.** Large-scale imaging of cortical network activity with calcium indicators. *Neurosci Res* 52: 132–138, 2005.
- Kerr JN, Greenberg D, Helmchen F.** Imaging input and output of neocortical networks in vivo. *Proc Natl Acad Sci USA* 102: 14063–14068, 2005.
- Kerr JN, de Kock CP, Greenberg DS, Bruno RM, Sakmann B, Helmchen F.** Spatial organization of neuronal population responses in layer 2/3 of rat barrel cortex. *J Neurosci* 27: 13316–13328, 2007.
- Koyama R, Muramatsu R, Sasaki T, Kimura R, Ueyama C, Tamura M, Tamura N, Ichikawa J, Takahashi N, Usami A, Yamada MK, Matsuki N, Ikegaya Y.** A low-cost method for brain slice cultures. *J Pharmacol Sci* 104: 191–194, 2007.
- Lips MB, Keller BU.** Activity-related calcium dynamics in motoneurons of nucleus hypoglossus from mouse. *J Neurophysiol* 82: 2936–2946, 1999.
- MacLean JN, Watson BO, Aaron GB, Yuste R.** Internal dynamics determine the cortical response to thalamic stimulation. *Neuron* 48: 811–823, 2005.
- Mao BQ, Hamzei-Sichani F, Aronov D, Froemke RC, Yuste R.** Dynamics of spontaneous activity in neocortical slices. *Neuron* 32: 883–898, 2001.
- Markram H, Helm PJ, Sakmann B.** Dendritic calcium transients evoked by single cavk-propagating action potentials in rat neocortical pyramidal neurons. *J Physiol* 485: 1–20, 1995.
- Moreaux L, Laurent G.** Estimating firing rates from calcium signals in locust projection neurons in vivo. *Front Neural Circuits* 1: 2, 2007.
- Morita M, Higuchi C, Moto T, Kozuka N, Susuki J, Itofusa R, Yamashita J, Kudo Y.** Dual regulation of calcium oscillation in astrocytes by growth factors and pro-inflammatory cytokines via the mitogen-activated protein kinase cascade. *J Neurosci* 23: 10944–10952, 2003.
- Murayama M, Miyazaki K, Kudo Y, Miyakawa H, Inoue M.** Optical monitoring of progressive synchronization in dentate granule cells during population burst activities. *Eur J Neurosci* 21: 3349–3360, 2005.
- Ohki K, Chung S, Ch'ng YH, Kara P, Reid RC.** Functional imaging with cellular resolution reveals precise micro-architecture in visual cortex. *Nature* 433: 597–603, 2005.
- Ohki K, Chung S, Kara P, Hubener M, Bonhoeffer T, Reid RC.** Highly ordered arrangement of single neurons in orientation pinwheels. *Nature* 442: 925–928, 2006.
- Ramdyia P, Reiter B, Engert F.** Reverse correlation of rapid calcium signals in the zebrafish optic tectum in vivo. *J Neurosci Methods* 157: 230–237, 2006.
- Sasaki T, Kimura R, Tsukamoto M, Matsuki N, Ikegaya Y.** Integrative spike dynamics of rat CA1 neurons: a multineuronal imaging study. *J Physiol* 574: 283–290, 2006.
- Sasaki T, Matsuki N, Ikegaya Y.** Metastability of active CA3 networks. *J Neurosci* 27: 517–528, 2007.
- Sato TR, Gray NW, Mainen ZF, Svoboda K.** The functional microarchitecture of the mouse barrel cortex. *PLoS Biol* 5: e189, 2007.
- Smetters D, Majewska A, Yuste R.** Detecting action potentials in neuronal populations with calcium imaging. *Methods* 18: 215–221, 1999.
- Smola A, Schölkopf B.** A tutorial on support vector regression. *Stat Comput* 14: 199–222, 2004.
- Sohya K, Kameyama K, Yanagawa Y, Obata K, Tsumoto T.** GABAergic neurons are less selective to stimulus orientation than excitatory neurons in layer II/III of visual cortex, as revealed by in vivo functional calcium imaging in transgenic mice. *J Neurosci* 27: 2145–2149, 2007.
- Stosiek C, Garaschuk O, Holthoff K, Konnerth A.** In vivo two-photon calcium imaging of neuronal networks. *Proc Natl Acad Sci USA* 100: 7319–7324, 2003.
- Takahashi A, Camacho P, Lechleiter JD, Herman B.** Measurement of intracellular calcium. *Physiol Rev* 79: 1089–1125, 1999.
- Takahashi N, Sasaki T, Usami A, Matsuki N, Ikegaya Y.** Watching neuronal circuit dynamics through functional multineuron calcium imaging (fMCI). *Neurosci Res* 58: 219–225, 2007.
- Thomas D, Tovey SC, Collins TJ, Bootman MD, Berridge MJ, Lipp P.** A comparison of fluorescent Ca²⁺ indicator properties and their use in measuring elementary and global Ca²⁺ signals. *Cell Calcium* 28: 213–223, 2000.
- Yaksi E, Friedrich RW.** Reconstruction of firing rate changes across neuronal populations by temporally deconvolved calcium imaging. *Nat Method* 3: 377–383, 2006.